D. Pérez-Estévez, J. Doval-Gandoy, A. G. Yepes, Ó. López and F. Baneira, "Enhanced Resonant Current Controller for Grid-Connected Converters With LCL Filter," in IEEE Transactions on Power Electronics, vol. 33, no. 5, pp. 3765-3778, May 2018, doi: 10.1109/TPEL.2017.2770218.

Enhanced Resonant Current Controller for Grid-Connected Converters With LCL Filter

Diego Pérez-Estévez, *Student Member, IEEE,* Jesús Doval-Gandoy, *Member, IEEE,* Alejandro G. Yepes, *Member, IEEE,* Óscar López, *Senior Member, IEEE,* Fernando Baneira, *Student Member, IEEE*

***Abstract*—Conventional resonant controllers (RCs) are commonly used in the current control of grid-tied converters with LCL filter due to their advantages, such as zero steady-state error at both fundamental sequences, easy design process, and straightforward implementation. Nevertheless, these traditional solutions do not permit to place the closed-loop poles of the system in convenient locations when dealing with a fourth-order plant model like the LCL filter plus the computation delay. Therefore, the reference tracking and the disturbance rejection are deficient in terms of transient behavior and depend on the LCL filter. Furthermore, an additional active damping method usually has to be designed in order to ensure stability. This article presents an enhanced current RC with stable and fast response, negligible overshoot, good disturbance rejection, and low controller effort for grid-tied converters with LCL filter. The developed solution uses a direct discrete-time pole-placement strategy from the classical control theory (using transfer functions), involving two extra filters, to enhance the performance of the RC. In this manner, the complexity of state-space methods from modern control theory is avoided. Simulation and experimental results are provided to verify the effectiveness of the proposed control scheme.**

***Index Terms*—Current control, grid-connected converter, LCL filter, parameter sensitivity, resonant controllers (RCs).**

I. Introduction

THE increasing popularity of renewable energy sources and distributed power generation systems [1] is imposing higher requirements on the grid-connected converters. Fast regulation is required to compensate for time-varying events (e.g., voltage sags or fluctuating output power of wind generation systems) [2], [3]. Among the different converter types, the voltage source converter (VSC) is commonly used in this type of applications due to its controllability, compact design, and ease of interface with power systems [4].

Manuscript received xxxxx; revised xxxxx; accepted xxxxx. Date of current version xxxxx. This work was supported by the Spanish Ministry of Science and Innovation and by the European Commission, European Regional Development Fund (ERDF) under project DPI2016-75832 and the FPI scholarship BES-2013-063149. Recommended for publication by Associate Editor xxxxx.

All the authors are with the Applied Power Electronics Technology Group (APET), University of Vigo, Vigo 36310, Spain (e-mail: dieperez@uvigo.es; jdoval@uvigo.es; agyepes@uvigo.es; olopez@uvigo.es; fbaneira@uvigo.es).

This paper has a supplementary downloadable video available at http://ieeexplore.ieee.org, provided by the authors. In this video, the experimental setup and the procedure to carry out the fifth test presented in the article is shown. This material is 276 MB in size.

Color versions of one or more of the figures in this paper are available online at http://ieeexplore.ieee.org.

Digital Object Identifier xxxxx

However, VSCs need a filter to attenuate the high-frequency switching currents. The LCL filter is the recommended option because of its compact size and good performance [5]. Contrarily to the attenuation of $20\,\mathrm{dB}$ per decade that a conventional L filter provides above its cutoff frequency, LCL filters attenuate the grid-side current with a slope of $60\,\mathrm{dB}$ per decade above their resonant frequency. This increased performance of the LCL filter is caused by its higher order [6].

A fundamental element that affects the performance of a grid-tied converter is the current controller. Among the several control structures that can be adopted, resonant controllers (RCs) are commonly used [3], [6]–[18]. They permit to control with zero steady-state error both the positive and the negative sequences of the current [7]. In addition, they offer an easy design process and a straightforward implementation. The previously proposed RCs (tuned at the fundamental frequency of the grid) can be classified into three main categories: proportional-resonant [6], [8]–[17]; vector proportional-integral [3]; and variations of these RCs, which improve the stability margins for certain LCL filters and for high ratios of fundamental-to-sampling frequency (e.g., by adding a phase compensation scheme [7], [18]). These references propose tuning methods for the controller gains but they do not guarantee a closed-loop pole position independent of the LCL filter used.

Traditional RCs do not have enough order (they are second-order transfer functions) to completely control the dynamics of such a relatively high-order plant model that comprises the LCL filter model plus the computation and modulation delays (one and a half samples, respectively [19]). In other words, this type of controller cannot arbitrarily establish the position of the closed-loop poles of the system, because their locations depend on the LCL filter installed. This degrades the reference-tracking and the disturbance-rejection responses of the system, and sometimes even the stability. Recently, the authors of [20] have proposed a transfer-function-based current controller for grid-tied inverters with an L filter that uses a direct pole-placement technique resulting in an enhanced transient response when compared to classic design. However, to the authors knowledge, a transfer-function-based pole-placement strategy has not yet been applied to a VSC with an LCL filter. When an LCL filter is considered, the strategy proposed in [20] is not suitable. In addition, it should be noticed that a pole-placement strategy is specially convenient in this case because of the reduced stability that results when an LCL filter is used with a classic design. This stability problem was analyzed in [10], where a threshold was found for the resonant frequency of the LCL filter: $f_s/6$ (with

f_s being the sampling frequency). Such critical frequency value determines the region where an additional damping mechanism is necessary just to achieve stability. When the grid-side current is controlled, the frequency region where conventional RCs are unstable is below $f_s/6$ [10].

Although the damping of the LCL filter can be implemented passively or actively, the latter is usually preferred, because passive damping causes extra losses and reduces the efficiency of the system [21]. The different active damping schemes can be classified according to the signal that is fed back. Commonly, the capacitor current [12], [15], [22], the capacitor voltage [8], [9], [13], or the grid-side current [16], [17], [23] are the variables involved in the damping scheme. However, these solutions need extra sensors or mechanisms to estimate the additional signals. This increases the complexity of the control, and some algorithms also have sensitivity problems and reduce the overall robustness of the system (e.g., derivative filtering of a signal usually increases the noise [9]). In addition, the active damping techniques only provide a stable system [8], [12], [13], [15]–[17], [22], [23], but they do not optimize the transient response in terms of controller effort, overshoot, axis decoupling, or speed. In order to avoid these problems, new solutions often resort to state-space controllers from modern control theory that have a more complex design process compared to conventional RCs [24].

Some of the proposed current RCs for VSCs with LCL filter control the converter-side current rather than the grid-side current [17]. However, in order to have a precise control of the power and distortion factors of the current injected into the grid, the grid-side current should be measured or estimated accurately [25]. A good estimation requires a precise model of the plant, which sometimes (especially in the case of VSCs connected to weak grids) is not available to the designer.

In addition, there is an increasing trend in the field of control of power converters that strives to achieve designs with faster dynamics (higher bandwidth) [3]; but sometimes such work comes from abstract mathematical proposals [13] where it is difficult to assess their practical and physical consequences in terms of controller effort and robustness to plant parameter variations and disturbances.

This paper presents an enhanced current RC for grid-connected converters with LCL filter. The proposed controller includes two filters that enhance the behavior of the system: a loop filter, which contains an RC and a prefilter. It is designed in a systematic way and gives a consistent (in agreement with the design) and fast transient response (using all the available bandwidth), with low controller effort, no overshoot, and a good robustness to disturbances and variations in the grid impedance, which makes it particularly suitable for operation in a weak grid. These improvements are achieved independently of the LCL-filter resonant frequency (above and below $f_s/6$) and sampling frequency used, and without adding an extra active damping method. The mathematical background of the presented current controller is based on a direct pole-placement strategy from the classical control theory (using transfer functions). The proposed design process overcomes the aforementioned problems of previously proposed RCs (i.e., the closed-loop poles are placed in convenient locations) and

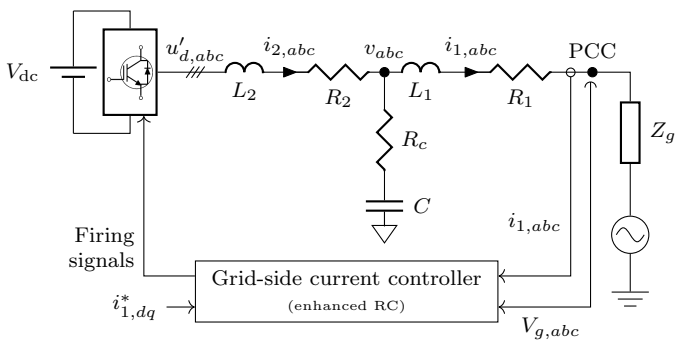

Fig. 1. Grid-connected VSC with an LCL filter and a grid-side current controller.

give a performance comparable to state-space controllers that use modern control theory [24], but based on a traditional control structure with a simpler design process and a lower computational load. Since transfer function control theory is typically used in the field of current controllers in power applications, this solution is more valuable for practicing power-electronic engineers or researchers. In addition, the assessment of robustness is commonly studied using a transfer function analysis [10], [20]. Another advantage of the proposal, compared to [24], is the huge reduction in the computational load, which makes the proposal particularly suited for an implementation in an embedded controller.

The rest of the paper is organized as follows. Section II introduces the model of the plant, the RC, and a feedforward. Then, in Section III, the loop filter and the prefilter are designed and the performance of the proposed current controller concerning its time response is analyzed. Next, in Section IV, its robustness to grid-impedance variations is assessed. In Section V, the theory is validated by simulation and experimental results. Finally, Section VI concludes the work.

II. Transfer-Function Modeling of the Plant and the Resonant Controller

This section presents the model of the augmented plant (i.e., including the RC) and the expression of a disturbance feedforward gain for the grid-side current controller shown in Fig. 1, where L_1, L_2, and C represent the reactive elements of the LCL filter; R_1, R_2, and R_c model the equivalent series resistances of the filter (R_2 also includes the equivalent loss resistance of the VSC [19]); $u'_{d,abc}$ is the VSC output voltage; $i_{1,abc}$, $i_{2,abc}$, and v_{abc} are the LCL-filter state variables (the grid-side current, the converter-side current, and the capacitor voltage, respectively); $V_{g,abc}$ is the grid voltage; and $i^*_{1,dq}$ denotes the grid-side current reference in the direct quadrature (dq) frame. The following modeling process successively calculates transfer functions that relate the variables of interest; each new transfer-function model is constructed from the model obtained in the previous stage. The resultant transfer function, denoted as augmented plant model, consists in an RC and the discrete model of the LCL filter plus the computation and modulation delays, and is calculated in Section II-A.

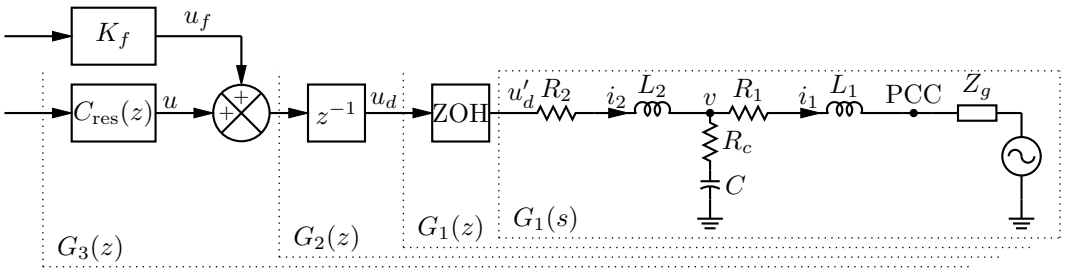

Fig. 2. Stationary-frame RC, grid-voltage feedforward, and plant diagram: LCL filter, PWM (modeled as a ZOH), and one-sample computation delay.

This transfer function is used later, in Section III, where the pole-placement is applied to design the remaining two filters of the controller. Finally, a feedforward gain to improve the disturbance rejection is calculated in Section II-B.

A. Model of the Augmented Plant

First, a continuous model that relates the grid-side current $i_1(t)$ to the VSC output voltage $u'_d(t)$ for the LCL filter shown in Fig. 2 is defined (when no reference frame in a subscript of a variable is detailed, the $\alpha\beta$ frame with an amplitude-invariant transformation is assumed). The grid impedance seen at the point of common coupling (PCC) Z_g is assumed to be zero in the model for the design of the controller because its value is unknown at the design stage (and often even variable); its effect is analyzed in Section IV. The resulting transfer function in continuous time that relates the converter output voltage u'_d with the grid-side current i_1 when the effect of the grid voltage V_g is not considered is

$$G_1(s) = \left.\frac{i_1}{u'_d}\right|_{\substack{V_g=0\\Z_g=0}} = \frac{Z_c}{Z_2(Z_1+Z_c)+Z_1Z_c} \tag{1}$$

where Z_1, Z_2, and Z_c are the impedances of the reactive elements including losses:

$$Z_1 = sL_1 + R_1, \quad Z_2 = sL_2 + R_2, \quad Z_c = 1/(sC) + R_c. \tag{2}$$

Next, (1) is discretized by using a zero-order-hold (ZOH) equivalent [26]. The effect of the zero-order hold is mainly to introduce a phase shift that corresponds to a time delay of $T_\mathrm{s}/2$ [26]. This discretization method takes into account the half a sample delay added by the pulse width modulator (PWM) [19]. The resulting model relates the PWM voltage reference (before the ZOH) $u_d(k)$ with the sampled grid-side current $i_1(k)$:

$$G_1(z) = \left.\frac{i_1}{u_d}\right|_{\substack{V_g=0\\Z_g=0}} = (1-z^{-1})\mathcal{Z}\left\{\mathcal{L}^{-1}\left[\frac{G_1(s)}{s}\right]\right\} \tag{3}$$

where $\mathcal{Z}\left[x(k)\right]$ and $\mathcal{L}\left[x(t)\right]$ denote the Laplace and Z transforms of the signal x, respectively. Then, a one-sample input (computation) delay is added to (3):

$$G_2(z) = z^{-1}G_1(z). \tag{4}$$

Furthermore, the RC $C_{\rm RC}(z)$, which eliminates any steady-state error in the grid-side current at the fundamental grid frequency ω_g, is

$$C_{\rm RC}(z) = \frac{1}{z^{-2} - 2\cos(\omega_g T_\mathrm{s})z^{-1} + 1}. \tag{5}$$

This transfer function places two conjugated open-loop poles at the fundamental grid frequency ω_g (i.e., at positions $z = e^{\pm j\omega_g T_\mathrm{s}}$, where $T_\mathrm{s} = 1/f_\mathrm{s}$ is the sampling period) so as to control both positive and negative sequences. No other poles or zeros are added to (5). Instead, the proposed controller defers to $C(z)$ and $H(z)$ the task of adding extra degrees of freedom. In this manner, the design process is simplified and a consistent performance is obtained independently of the LCL filter used.

Hence, the model of the augmented plant (i.e., including the RC), depicted in Fig. 2, is

$$G_3(z) = C_{\rm RC}(z)G_2(z). \tag{6}$$

B. Disturbance Feedforward

A feedforward of the grid voltage V_g is implemented (cf. Fig. 2) to improve the disturbance rejection and provide a smooth start of the converter. Nevertheless, when a weak grid is considered, the voltage feedforward can be reduced to improve the robustness, as explained in Section IV. Therefore, in this case, the authors recommend removing the voltage feedforward by setting K_f to zero. When the controller output u is zero, the capacitor voltage v should be equal to the grid-side voltage V_g in order for the grid-side current to be zero $i_1 = 0$. Consequently, the necessary feedforward voltage that should be generated at the converter output u'_d is

$$u'_d = \frac{(Z_2+Z_c)V_g}{Z_c}. \tag{7}$$

If the effect of computation and modulation delay is compensated at the fundamental grid frequency component in the feedforward voltage u_f, then the resultant feedforward gain is

$$K_f = \frac{u_f}{V_g} = \frac{(Z_2+Z_c)e^{j1.5\omega_g T_\mathrm{s}}}{Z_c}. \tag{8}$$

III. Design of Loop Filter and the Prefilter

The proposed controller (shown in Fig. 3) uses an output error feedback structure involving a loop filter and a prefilter [26]. The loop filter consists in two transfer functions, namely, $C(z)$ and $C_{\rm RC}(z)$; and the prefilter is $H(z)$.

$C(z)$ and $H(z)$ are described throughout this section. With the developed scheme, only the grid-side current $i_{1,abc}$ and

Since zero-sequence current cannot flow, two current sensors are enough.

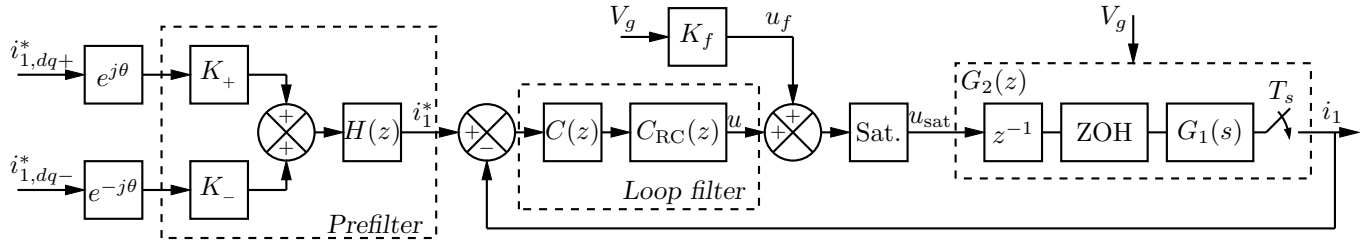

Fig. 3. Scheme of the model of the plant and the proposed controller structure.

the grid voltage $V_{g,abc}$ are measured. These variables are transformed to the $\alpha\beta$ frame, resulting in i_1 and V_g. The grid-side current references of the current controller in the positive- and negative-sequence dq frames are $i^*_{1,dq+}$ and $i^*_{1,dq-}$, respectively. They are transformed to the $\alpha\beta$ frame before they are applied to the prefilter. The phase of the positive-sequence fundamental grid voltage θ is estimated by a phase-locked loop (PLL). The feedforward u_f of the grid voltage V_g is added at the controller output u. Finally, the resulting sum is saturated (to take such effect of the modulator into account), obtaining the saturated PWM voltage reference u_{sat}. In the following, the two filters $C(z)$ and $H(z)$ that are included in the controller (in addition to the RC) are designed. However, in order to obtain a good design, a previous knowledge of the bandwidth of the plant is required to define the dominant frequency of the system.

A. Assessment of the Dominant Frequency of the System According to the Available Bandwidth

As mentioned in the Introduction, the physical and practical implications of the design decisions, such as the bandwidth of the controller, should not be hidden behind the mathematical formulation. The response to broadband signals like sags or reference current changes is determined by the bandwidth of the controller. If a high bandwidth is set in the controller, fast references (high frequencies) can be followed. Regarding disturbances, a fast compensation is obtained. However, a fundamental fact about power-system models is that they do not exhibit good frequency response fidelity with the real power system beyond a certain frequency. This is due to plant parameter variations, unmodeled dynamics, power limits, or nonlinearities, to name a few. Here, the focus is placed on the voltage limits of the VSC (represented by the saturator in Fig. 3) in relation with the low-pass characteristics of the LCL filter. In the following, an analysis of the current slew-rate limitation and its implications on the current controller is presented. Since the LCL filter heavily blocks the grid-side current above the resonant frequency ω_{res}, the VSC needs to generate a high actuation (possibly entering into overmodulation) when high frequencies (fast signals) are commanded [24]. This limitation does not depend on the type of control scheme adopted, but on the LCL filter and dc-bus voltage of the VSC.

The VSC output voltage is bounded and depends on the dc-bus voltage V_{dc}. The maximum amplitude of the voltage step that the VSC can apply per phase to the LCL filter (in the linear region of the PWM) is $u'_{d,\max} - V_g = (2/3)V_{\mathrm{dc}} - V_g$. The slew rate S_r (defined as the rate of change of current per unit of time, i.e., the time differentiation of i_1) that this step generates in the grid-side current is

$$S_r = \frac{z-1}{T_{\mathrm{s}}} I_1(z) = \underbrace{\frac{z-1}{T_{\mathrm{s}}}}_{\text{Time diff.}} \underbrace{\left(\frac{2V_{\mathrm{dc}}}{3} - V_g\right)\frac{z}{z-1}}_{\text{Voltage step}} \underbrace{G_1(z)}_{\text{LCL filter}} . \quad (9)$$

On the other hand, a sinusoid of frequency f_{dom} and amplitude A_p has a maximum slew rate of $S_r^{\sin} = 2\pi f_{\mathrm{dom}} A_p$. In this manner, the bandwidth of the current controller should be set according to the amplitude A_p and slope $S_r^{\sin}$ of the maximum expected current references and never exceed the bandwidth in the real open-loop system, which is limited by the slew rate (9). Therefore, the available bandwidth is

$$\mathrm{BW_A} = \frac{S_r}{2\pi A_p}. \quad (10)$$

This value yields an upper limit for the dominant frequency of the system f_{dom}. In order to ensure a negligible effect of the damped resonant poles of the LCL filter on the system response (as demonstrated later in Section V), the following condition should also be met: $f_{\mathrm{dom}} \leq f_{\mathrm{res}}/2$ [24]. Therefore, the proposed controller has a dominant pole at a natural frequency

$$f_{\mathrm{dom}} \leq \min\left\{\frac{S_r}{2\pi A_p}, \frac{f_{\mathrm{res}}}{2}\right\}. \quad (11)$$

B. Closed-Loop Pole Placement by Means of $C(z)$

The proposed pole location aims to give a constant and predictable system performance, in combination with low controller effort, irrespectively of the LCL filter used. $C(z)$ is the part of the controller transfer function that is used to place the closed-loop poles of the system in the desired locations, and it is calculated according to the proposed pole-placement strategy.

The desired closed-loop pole locations are defined in the following. The number of closed-loop poles of the complete system is nine: four poles from the plant $G_2(z)$, two poles from the RC $C_{\mathrm{RC}}(z)$, and three poles from the controller $C(z)$. Therefore, nine closed-loop pole positions should be defined.

On the one hand, the transfer function of the plant model (4) has four (open-loop) poles, which have a direct relation with the physical system. Three of these poles model the

The synchronous frames permit an independent control of the active and reactive power.

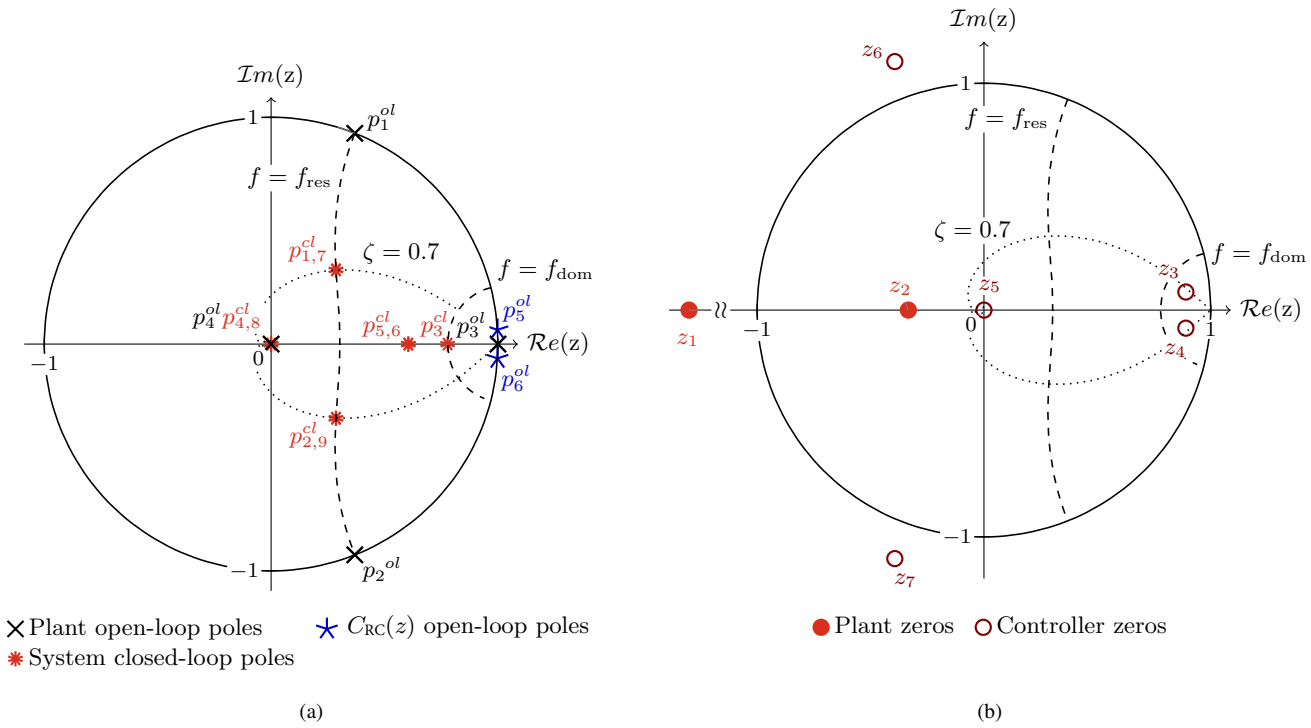

(a) (b)

Fig. 4. Roots of the complete closed-loop system (without the prefilter). (a) Pole map (includes the open-loop poles of the plant and of the RC). (b) Zero map.

LCL filter, which has two complex conjugate poles $p_{1,2}^{ol}$ (its resonant poles) at the resonant frequency and a real pole p_3^{ol} at zero frequency. The fourth pole p_4^{ol} models the computation delay and it is placed at the origin of the z-plane. These four poles are shown in Fig. 4(a), which depicts the pole map of the system. To maintain the required controller effort low, the closed-loop poles related to a physical system (as in this case) should be kept close to the corresponding open-loop poles whenever the response is not significantly degraded [24], [26].

The two resonant poles of the LCL filter impose serious limitations on the transient response. In order to provide a good response and keep the control effort low, a radial projection [26] of the resonant poles of the plant is used. This technique minimizes control usage by simply adding damping (a damping factor ζ of 0.7 is used) to lightly-damped open-loop poles without changing their natural frequency [26] [cf. $p_{1,2}^{cl}$ in Fig. 4(a)].

The third pole of the LCL filter p_3^{ol} is displaced to a higher natural frequency [see p_3^{cl}, in Fig. 4(a)] and is set to be the dominant pole of the system. A natural frequency f_{dom} [cf. (11)] is recommended for the dominant pole p_3^{cl}, as obtained from the available-bandwidth analysis.

The delay pole p_4^{ol} is not moved because it is already in an optimum location (at the origin of the z-plane).

On the other hand, the rest of the poles do not correspond to any physical system: $p_{5,6}^{ol}$, the two resonant poles of $C_{\text{RC}}(z)$; and $p_{7,8,9}^{ol}$, the three poles of $C(z)$. Hence, the locations of these poles are not restricted to yield a low control effort. Therefore, a larger bandwidth (faster poles) can be set. In this manner, it is advisable to place the corresponding closed-loop poles ($p_{5,6,7,8,9}^{cl}$) at natural frequencies higher (and sufficiently damped) than that of the dominant pole p_3^{cl} so as to ensure that the system dynamics are similar to those of this pole alone [26]. The locations already defined for $p_{1,2,4}^{cl}$ are also assigned to these closed-loop poles (cf. Table I). An analogous reasoning was applied in [24] to place the poles of the observer in a state-feedback controller.

Table I summarizes the proposed locations for the closed-loop poles of the plant and the controller. Appendix A presents the mathematical details of the pole-placement design method applied to the system, so that the poles are effectively placed in such desired locations. In addition, the computational load of the proposed controller is given in Appendix B.

As mentioned in Section I, the design process is straightforward compared with other techniques, because of the use of a direct discrete-time pole-placement strategy. The poles are in the desired locations [cf. Table I] provided that the grid impedance is zero, because the design process takes into account the resonant frequency of the LCL filter.

C. Prefilter for Eliminating the Slow Zeros

Although the location of the poles determines the system modes, it is the location of the zeros which determines the proportion in which these modes are combined in order to produce the system response [26].

On the one hand, the LCL filter model (1) does not have any zeros. However, all discrete-time models obtained by discretization of continuous ones turn out to have relative

The system modes of a linear system determine the system behavior. Any zero-input response of a linear system is a linear combination of its system modes [26].

TABLE I
POLE PLACEMENT

Poles	Position in the z-plane	
	Open-loop	**Closed-loop**
$G_1(z)$ **LCL filter**	Radial projection of resonant poles to $\zeta = 0.7$.	
	$p_{1,2}^{ol} = e^{\pm j\omega_{\text{res}} T_s}$	$p_{1,2}^{cl} = e^{-(\zeta\omega_{\text{res}} \pm j\omega_{\text{res}}\sqrt{1-\zeta^2})T_s}$
	Moved to make it the dominant pole, with a high bandwidth.	
	$p_3^{ol} = 1$	$p_3^{cl} = e^{-\omega_{\text{dom}} T_s}$
Comp. delay	Not moved; already in a fast and damped location.	
	$p_4^{ol} = 0$	$p_4^{cl} = 0$
$C_{\text{RC}}(z)$ **Resonant controller**	Moved to twice the frequency of the dominant pole.	
	$p_{5,6}^{ol} = e^{\pm j\omega_g T_s}$	$p_{5,6}^{cl} = e^{-2\omega_{\text{dom}} T_s}$
$C(z)$ **controller**	Placed at natural frequencies higher (and sufficiently damped) than that of the dominant pole p_3^{cl}. The open-loop pole positions of $C(z)$ (the roots of its denominator) are obtained from its denominator coefficients n_0, n_1, n_2, and n_3, which are given in Appendix A.	
	$p_{7,8,9}^{ol} = \texttt{roots}([n_3, n_2, n_1, n_0])$	$p_{7,9}^{cl} = p_{1,2}^{cl} \quad p_8^{cl} = p_4^{cl}$

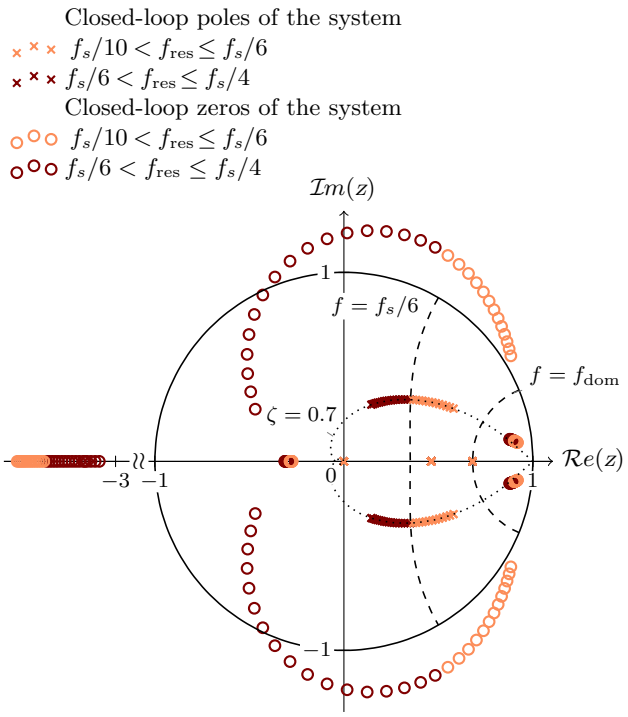

Fig. 5. Root locus of the closed-loop system (without the prefilter) for a sweep in the resonant frequency of the LCL filter.

degree one, irrespective of the relative degree of the original continuous system [27]. The relative degree of a transfer function is the difference between the degree of the denominator (number of poles) and that of the numerator (number of zeros). Therefore, when the third-order LCL filter model is discretized, two fast (placed at much higher natural frequencies than the dominant pole) zeros $z_{1,2}$ appear. These sampling zeros (introduced by the discretization process [28]) should never be canceled or compensated [27], in order to avoid high-frequency oscillations. Fig. 4(b) shows the zero map of the closed-loop system, where these zeros can be seen.

On the other hand, the controller $C(z)$ has five zeros [cf. Fig. 4(b)]: two slow zeros (much closer to the stability boundary than the system dominant pole) $z_{3,4}$, one fast zero z_5, and two non-minimum-phase zeros $z_{6,7}$ whose location varies significantly with the resonant frequency of the LCL filter. This variation in the location of the zeros is shown in Fig. 5, which depicts the root locus of the closed-loop system for a sweep in the resonant frequency of the LCL filter.

In order to obtain a good transient response, it should be ensured that there are no zeros with natural frequencies below that of the dominant pole [27]. The effect of the zeros $z_{1,2,5,6,7}$ on the response is negligible because they are placed in regions of natural frequencies above that of the dominant pole. However, there are two slow zeros, $z_{3,4}$ [cf. Figs. 4(b) and 5], which should be removed. Hence, the following prefilter $H(z)$ is added, as depicted in Fig. 3, in order to cancel the two slow zeros $z_{3,4}$ with two additional poles:

$$H(z) = \frac{z}{(z - z_3)(z - z_4)}. \tag{12}$$

The added zero at the origin cancels p_4^{cl}; hence, the system response is one sample faster. This prefilter also modifies the gain and phase of the closed-loop system at the grid frequency; therefore, a pair of complex gains K_+ and K_- are added (cf. Fig. 3) to restore the unity gain:

$$K_+ = \frac{1}{H(e^{j\omega_g T_s})} \quad \text{and} \quad K_- = \frac{1}{H(e^{-j\omega_g T_s})}. \tag{13}$$

In summary, the controller changes the dynamics of the open-loop plant to the desired closed-loop dynamics. The open-loop plant model $G_2(z)$ does not have a flat frequency response. It has a pole at dc and two complex-conjugate poles at the resonant frequency of the LCL filter, cf. Fig. 6. When the loop filter is installed, the closed-loop transfer function of the system is

$$G_{\text{cl}}(z) = \frac{i_1}{i_1^*}\bigg|_{V_g=0} = \frac{C(z)G_{\text{RC}}(z)G_2(z)}{1 + C(z)G_{\text{RC}}(z)G_2(z)}. \tag{14}$$

This transfer function has a damped response, as expected from the proposed closed-loop poles locations, cf. Fig. 6. Nevertheless, the obtained response still does not have the desired flat low-pass response. $C(z)$ introduces two slow zeros at a frequency f_{sz} that is lower than the frequency of the dominant pole of the system f_{dom}. These zeros are the cause of the swell in the frequency response of the system. By adding the prefilter, the desired closed-loop response is obtained, cf. Fig. 6. The final bandwidth of the current controller is slightly less than the specified f_{dom} because of the extra non-dominant poles of the system; however, the response approximates accurately that of a first order of system.

IV. SENSITIVITY TO GRID-IMPEDANCE VARIATIONS

The robustness analysis to the grid impedance is structured into three parts. In the first place, the parameters involved in

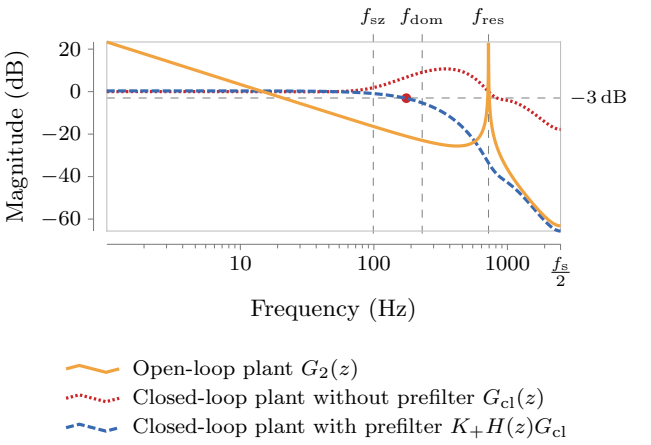

Fig. 6. Effect of the proposed controller on the LCL-filter resonance frequency is analyzed through Bode magnitude plots.

the analysis are discussed. This permits to generalize the conclusions obtained to any LCL filter and sampling frequency. In the second place, a robustness analysis is carried out using a Nyquist diagram to obtain the phase and gain margins of the system for all combinations of LCL filter values and sampling frequencies. A frequency region $1/10 \leq f_{res}/f_s \leq 1/4$, which includes the different regions established in [10], is chosen. In the third place, the effect of the grid impedance on the gain and phase margins of the system is analyzed. Such analysis gives an insight to the previous mathematical results and helps to understand the practical implications of increasing the grid impedance.

In order to analyze the robustness of the proposed controller to variations in the grid impedance, first, the parameters involved in the analysis need to be presented. The open-loop transfer function (OLTF) is the transfer function that determines the stability of the system. It is the transfer function where the gain and phase margins of the system are calculated, and also where the Nyquist stability criterion is applied. The OLTF of the proposal is the product of the loop filter times the discrete-time plant model (cf. Fig. 3):

$$\text{OLTF} = \underbrace{C(z)C_{\text{RC}}(z)}_{\text{Loop filter}} G_2(z). \tag{15}$$

The plant model depends on seven parameters: the filter reactive values L_1, L_2, and C; the equivalent series resistances (ESRs) R_1, R_2, and R_c; and the sampling frequency f_s. In addition, the designer also specifies an extra parameter f_{dom}, which sets the desired bandwidth of the current controller. In order to reduce the number of parameters in the robustness analysis, the ESRs of the LCL filter are considered to be zero. This simplification assumes a high-quality-factor resonant LCL filter, which is a worst-case scenario in terms of stability. The ESRs damp the resonant poles and the dc pole of the LCL filter and yield a more stable filter. Therefore the results and conclusions derived in this analysis can also be applied to lower-quality-factor LCL filters. The parameter f_{dom} is defined as one third of the resonant frequency of the LCL filter for the analysis.

Although the physical nature of the problem can be best understood in terms of the physical parameters (L_1, L_2, C_f), it is the frequency-domain parameters (poles and zeros) that best serve the purpose of this first part of the robustness analysis. If the ESRs are assumed to be zero, then the discrete-time plant model [cf. (4)] can also be expressed in the zero-pole-gain form as

$$G_2(z) = \overbrace{K}^{\text{Gain}} \frac{\overbrace{(z-z_1)(z-z_2)}^{\text{Sampling zeros}}}{\underbrace{z}_{\text{Comp. delay}} \underbrace{(z-1)}_{\text{DC pole}} \underbrace{(z-p_1^{\text{ol}})(z-p_2^{\text{ol}})}_{\text{Resonant poles}}}. \tag{16}$$

This model has one pole at dc, $z = 1$; one pole at the origin, which models the computational delay; two resonant poles $p_{1,2}^{\text{ol}}$ [cf. Fig. 4(a)]; two sampling zeros $z_{1,2}$ [cf. Fig. 4(b)]; and a constant gain K to complete the zero-pole-gain form of the model. The location of both $p_{1,2}^{\text{ol}}$ and $z_{1,2}$ depends on the ratio of the LCL-filter resonant frequency to sampling frequency f_{res}/f_s.

The proposed controller design gives a loop filter that yields the same closed-loop poles (cf. Table I) irrespectively of the particular value of K, due to the pole-placement strategy. In this manner, the OLTF does not depend on the value of the gain K neither. Therefore, although the OLTF seems to depend on many parameters, it is the ratio of the LCL-filter resonant frequency to sampling frequency f_{res}/f_s the one that should be varied in the robustness analysis.

The developed robustness analysis is conducted for a wide sweep of such parameter: $1/10 \leq f_{res}/f_s \leq 1/4$, which includes the value $1/6$, where conventional resonant controllers become unstable [10]. Fig. 7 shows the Nyquist diagram and the associated phase and gain margins of the system for a f_{res}/f_s sweep. The Nyquist diagram goes several times to infinity because of the infinite gain of the OLTF at the grid frequency, at dc, and at the resonant frequency of the LCL filter. Therefore, in order not to clutter the diagram, only the part of the plot that corresponds to positive frequencies and is closest to the point -1 is depicted (the part that corresponds to the negative frequencies is a mirror image). The results show that the encirclement of the point -1 is performed with an approximately constant radius. Therefore, there are no sensitivity peaks [7] in the response. Furthermore, the results are consistent in spite of the large variation in the ratio f_{res}/f_s, as expected from the design process.

This analysis also gives a mathematical assessment of the well-known fact that the design of the current controller becomes more difficult as the resonant frequency of the LCL filter approaches the Nyquist frequency ($f_s/2$), because the robustness of the system is degraded. Nevertheless, such mathematical results do not convey a good understanding of the robustness to a variation in a physical parameter such as the grid impedance. In order to tackle this problem, a careful study of the effect of such parameter, in terms of gain and phase margins, is presented next.

The previous stability margins correspond to a system where the grid impedance is zero, i.e., with nominal plant parameters.

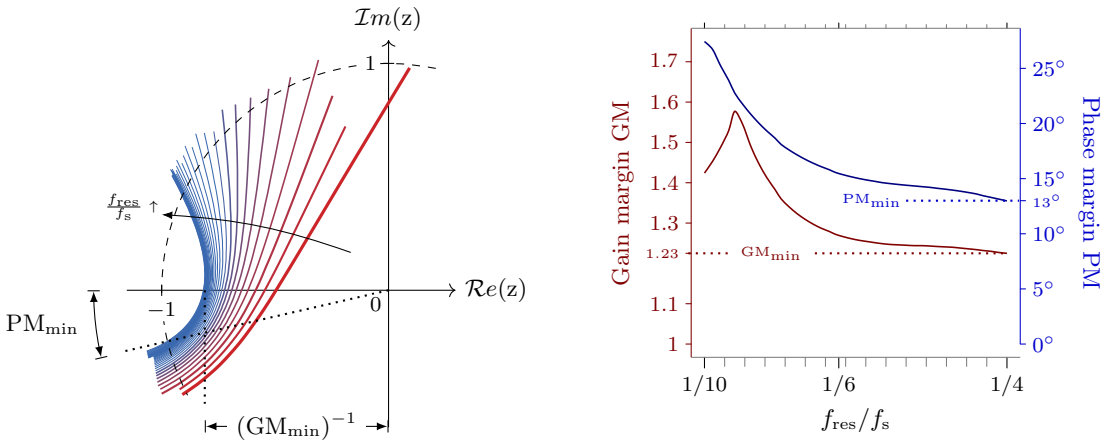

(a) (b)

Fig. 7. Robustness analysis for a sweep in the ratio f_{res}/f_s from $1/10$ to $1/4$. (a) Nyquist diagrams. (b) Stability margins.

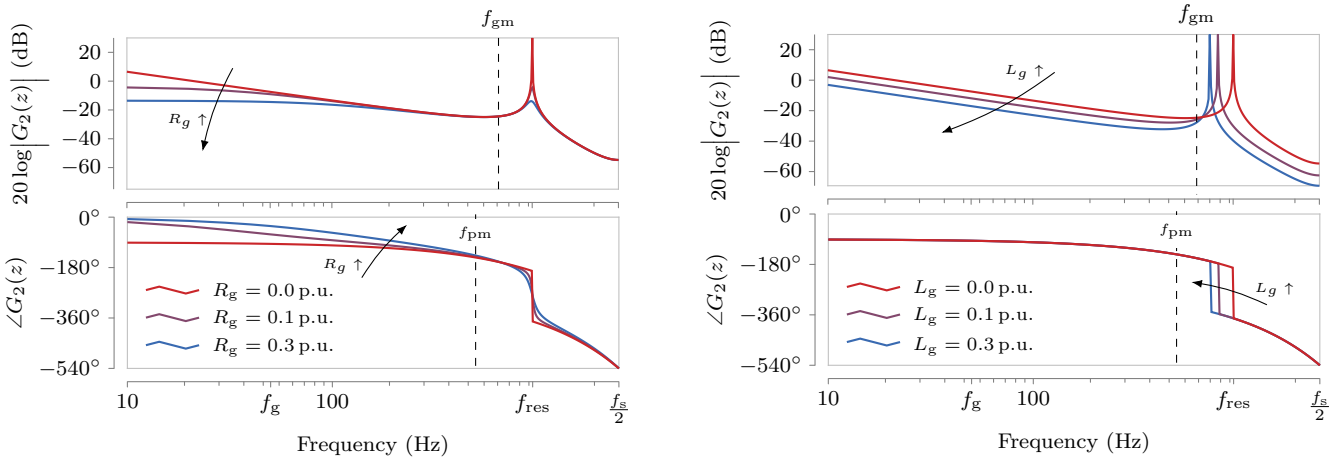

(a) (b)

Fig. 8. Effect of the grid impedance on the plant model. (a) Effect of R_g ($L_g = 0$). (b) Effect of L_g (R_g=0).

PLACE HOLDER FOR PHASE PLOT

When a nonzero grid impedance is considered and the voltage feedforward is removed, the continuous plant model becomes

$$G_1(s, R_g, L_g) = \left.\frac{i_1}{u'_d}\right|_{\substack{V_g=0 \\ K_f=0}} = \frac{Z_c}{Z_2(Z_1 + Z_g + Z_c) + (Z_1 + Z_g)Z_c} \quad (17)$$

where

$$Z_g = R_g + sL_g, \quad Z_1 = sL_1, \quad Z_2 = sL_2, \quad Z_c = 1/(sC). \quad (18)$$

This last part of the robustness study resorts to a numerical evaluation of the discrete plant model $G_2(z)$ obtained from the modified continuous plant model (17) for a set of representative grid-impedance values and the parameters of LCL filter I from Table II. Such study permits to obtain an insight into the problem and avoid the complexity of an analytical analysis.

Fig. 8 shows the frequency response of the discrete-time plant model $G_2(z)$ when the reactive and ohmic components of the grid impedance are independently increased. For a clearer evaluation of their effect, the ohmic and reactive components of the grid impedance are discussed separately. First, the effect of R_g is discussed assuming that L_g is zero. Then, L_g is modified while R_g is zero.

On the one hand, Fig. 8(a) shows that if R_g is increased, then the magnitude of the plant model is reduced, especially at the highest-gain frequency ranges, namely at dc and at the resonant frequency. At the phase crossover frequency f_{gm}, the frequency where the gain margin is measured, the magnitude change is minimum; hence, robustness is maintained. In order to assess the effect of R_g on the phase of the OLTF, it is important to recall that, in an inductor, current lags voltage by 90°, whereas in a resistor, both magnitudes are in phase. Therefore, increasing R_g while L_g is kept constant also reduces the phase lag of the system at a wide range of frequencies, including the gain crossover frequency f_{pm}, the frequency where the phase margin is measured. This improves the stability, as expected from the higher damping of the system.

On the other hand, Fig. 8(b) shows that increasing L_g has a similar effect to rising R_g because it also boosts the overall impedance of the filter. Therefore, a lower magnitude in the

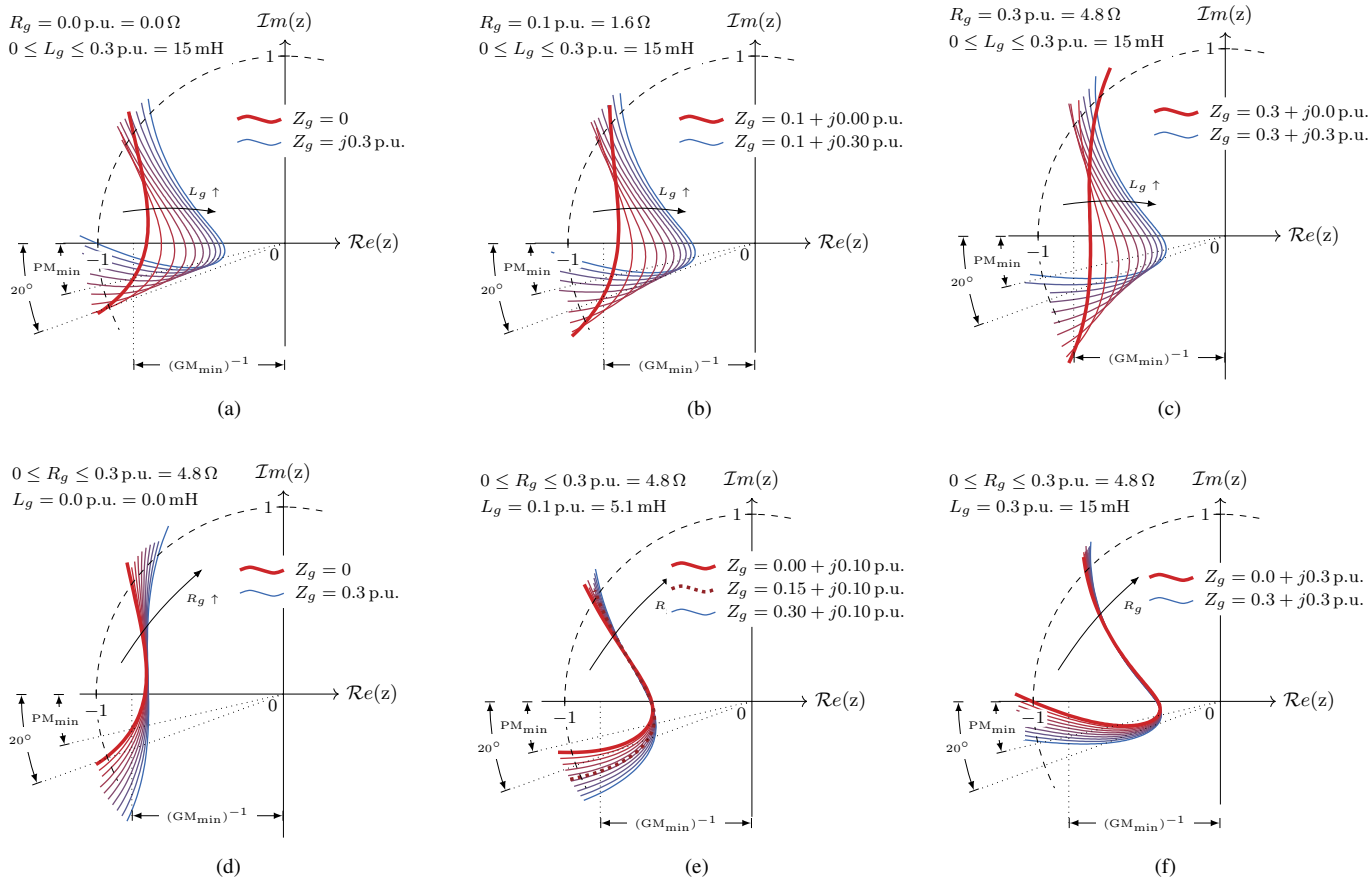

Fig. 9. Nyquist diagram of the system that shows the effect of the grid impedance on the OLTF. (a)-(c) Sweep in L_g while R_g is kept constant. (d)-(f) Sweep in R_g while L_g is kept constant.

plant model (and in the OLTF) is obtained. However, increasing the grid inductance also lowers the resonant frequency of the system. When the resonant frequency is lowered, the gain of the OLTF dramatically increases at the frequency of the new resonant frequency. If this change in the resonant frequency is big enough to reach the phase crossover frequency, then the system becomes unstable, because there is no gain margin large enough to compensate for the infinite gain of an LCL filter at the resonant frequency.

In order to complete the analysis, Fig. 9 shows the resultant Nyquist diagram when both the reactive and ohmic components are modified simultaneously. On the one hand, Figs. 9(a)-(c) display the effect of increasing the grid inductance from zero to a value of 0.3 p.u. for three values of grid resistance ($0, 0.1,$ and 0.3 p.u.). On the other other hand, Figs. 9(d)-(f) present the effect of increasing the grid resistance from zero to a value of 0.3 p.u. for three values of grid inductance ($0, 0.1,$ and 0.3p.u.). As indicated above, increasing R_g results in greater system stability whereas rising L_g improves the gain margin but reduces the phase margin because of the change in the resonant frequency. When L_g is 0.3 p.u. and R_g is zero, the system reaches the stability boundary.

As a conclusion from the numerical results, a brief qualitative analysis is presented here. For a given modulator reference voltage u, the grid-side current is usually reduced as the grid impedance is increased (Ohm's law). Therefore, increasing the grid impedance has a similar effect to reducing the controller gain, which typically increases the stability of a system. There are some subtleties which are neglected in this simple reasoning; hence, a complete and careful study of the numerical results is recommended for a comprehensive understanding of the problem. In order to drive the system into instability, a value of L_g equal to $0.3\,\text{p.u.}$ is required, which is higher than the inductance of a properly designed LCL filter. Since during normal operation the grid impedance is much lower than such value, it can be concluded that the proposed controller is robust to changes in the grid impedance. When the grid impedance becomes greater than such a large value, e.g. during islanded operation, a voltage controller should be used in place of a current controller.

V. Simulation and Experimental Results

The experimental results are carried out in a 10-kW VSC working as an inverter with a dc-bus voltage of $V_{\text{dc}} = 730\,\text{V}$ and connected to a 400-V line-to-line three-phase grid of $50\,\text{Hz}$. The switching frequency is $f_{\text{sw}} = 2.5\,\text{kHz}$, and the dead-time is $3\,\mu\text{s}$. A double-update sampling strategy is used, resulting in a sampling frequency f_{s} of $5\,\text{kHz}$. Two LCL filters with different resonant frequencies f_{res} (above and below the threshold $f_{\text{s}}/6$ [10]) are used to connect the VSC to the grid.

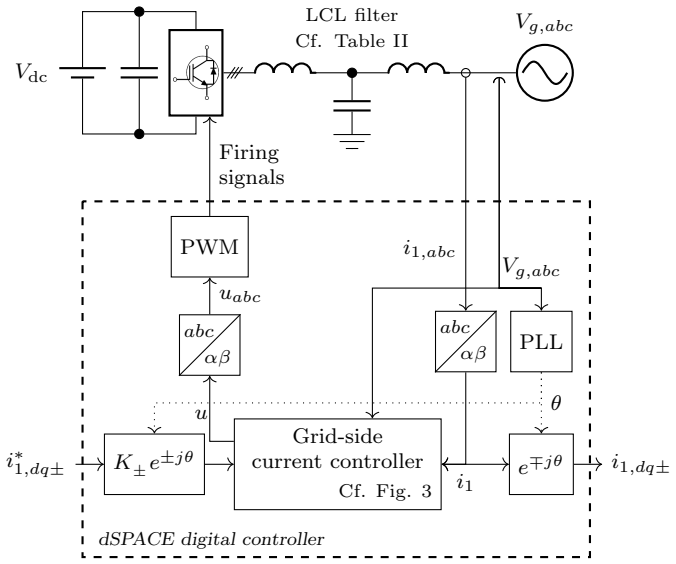

(a)

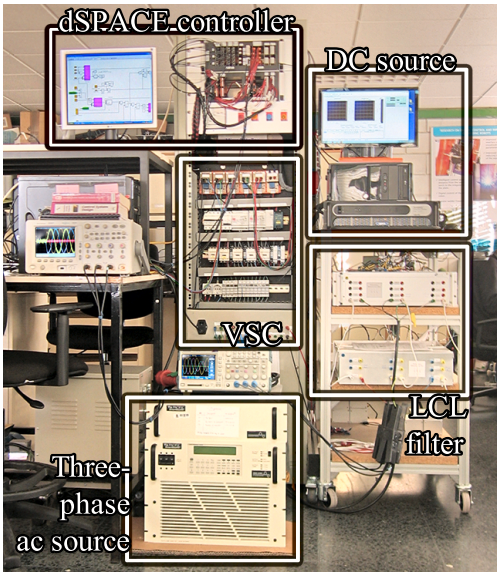

(b)

Fig. 10. Experimental setup of the grid-connected inverter. (a) Diagram. (b) Photograph.

The filter parameters are presented in Table II. Filter I was designed according to [29] in order to obtain a high filter performance in combination with low reactive values. The available bandwidth [cf. (10)] with filter I and filter II is 230 Hz and 200 Hz, respectively, according to Section III-A ($A_p = 10$ A and $S_r = 14500\,\mathrm{A/s}$ for filter I, and $S_r = 12500\,\mathrm{A/s}$ for filter II). The implemented controllers are designed using the proposed method with a dominant frequency equal to the available bandwidth. Figs. 10(a) and 10(b) show a diagram and a photograph of the experimental setup, respectively. In addition, a video demonstration that the authors feel it would enhance the reader's understanding of the research contribution has also been included.

The reference tracking (of both sequences) and the disturbance rejection (of both sequences) are tested for each of the

TABLE II
LCL Filter, ESRs, and Grid Impedance Parameters

	Param.	Filter I	Filter II
	L_1	3.75 mH, 0.07 p.u.	5.4 mH, 0.11 p.u.
	L_2	3.75 mH, 0.07 p.u.	5.4 mH, 0.11 p.u.
	C	15 μF, 0.07 p.u.	18 μF, 0.09 p.u.
	f_{res}	950 Hz	722 Hz
ESRs	R_1	0.5 Ω, 0.03 p.u.	0.5 Ω, 0.03 p.u.
	R_2	1.0 Ω, 0.06 p.u.	1.0 Ω, 0.06 p.u.
	R_c	0.1 Ω, 0.01 p.u.	0.1 Ω, 0.01 p.u.
$\mathbf{Z_g}$	R_g	2.5 Ω, 0.15 p.u.	
	L_g	5.4 mH, 0.10 p.u.	

LCL filters [Figs. 11(a)–14(a) for LCL filter I, and Figs. 11(b)–14(b) for LCL filter II]. Fig. 15 tests the robustness of the controller to an increase in the grid inductance (filter I is used). In all the tests, the controller achieves zero steady-state error at both fundamental sequences thanks to the action of the resonant controller $C_{\mathrm{RC}}(z)$.

Discrete-time linear simulations obtained with Matlab are shown superimposed to the experimental results. The oscilloscope captures show the reference signal i_1^*, the simulated response i_1^{sim}, and the measured response i_1. The experimental response accurately matches that predicted by the simulation, as shown in Figs. 11–14, in spite of it using a simple linear averaged model. The minor differences that appear between the simulated and the measured grid-side current are caused by nonidealities not taken into account in the system model, such as the nonlinear nature of the VSC.

First, the reference-tracking capability of the system is shown in Figs. 11 and 12. In order to test the transient response of the current controller, a reference step in the d axis is generated. Fig. 11 shows this reference step for the positive-sequence dq frame (dq+). The measured currents $i_{1,abc}$ are also transformed to a synchronous frame rotating at the same frequency. This transformation permits to measure the transient-response parameters (rise time, settling time and overshoot) in the variable $i_{1,dq}$. The 10%–90% rise time of the experimental response i_1 in Fig. 11 is approximately 1.5 ms for filter I and 1.75 ms for filter II. These values are in accordance with those of a first-order system of the same bandwidth, $T_{10\%-90\%} = 2.2/(2\pi f_{\mathrm{dom}})$. Negligible overshoot and good axis decoupling are attained because the response is mainly determined by the well-damped dominant closed-loop pole p_3^{cl} (see Fig. 4) placed at the natural frequency f_{dom}. Next, Fig. 12 shows a reference step of the same amplitude, but now in the negative-sequence dq frame (dq−). The obtained response has roughly the same transient-response parameters as in Fig. 11, because the proposed enhanced RC manages to treat both sequences in the same manner.

Next, the disturbance-rejection capability of the controller to sags in the grid voltage is assessed. Sags usually cause unbalanced voltage grid conditions. In particular, a 40%-depth type-C sag [30], which contains both voltage sequences, is generated with a three-phase ac voltage source for the remaining tests. In the first disturbance test (see Fig. 13), the current reference $i_{1,dq+}^*$ is kept constant. The settling time

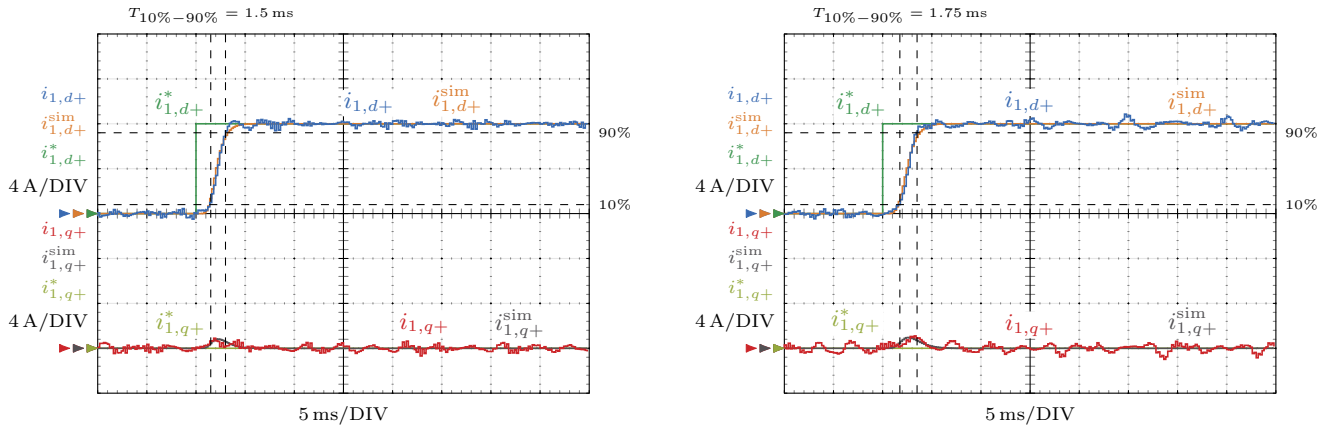

(a) (b)

Fig. 11. Experimental and simulation waveforms ($i_{1,dq}$ and $i^{\text{sim}}_{1,dq}$, respectively) for a reference step $i^{*}_{1,q+}$ in the positive synchronous frame dq+ rotating at the fundamental grid frequency ω_g. (a) LCL filter I (b) LCL filter II.

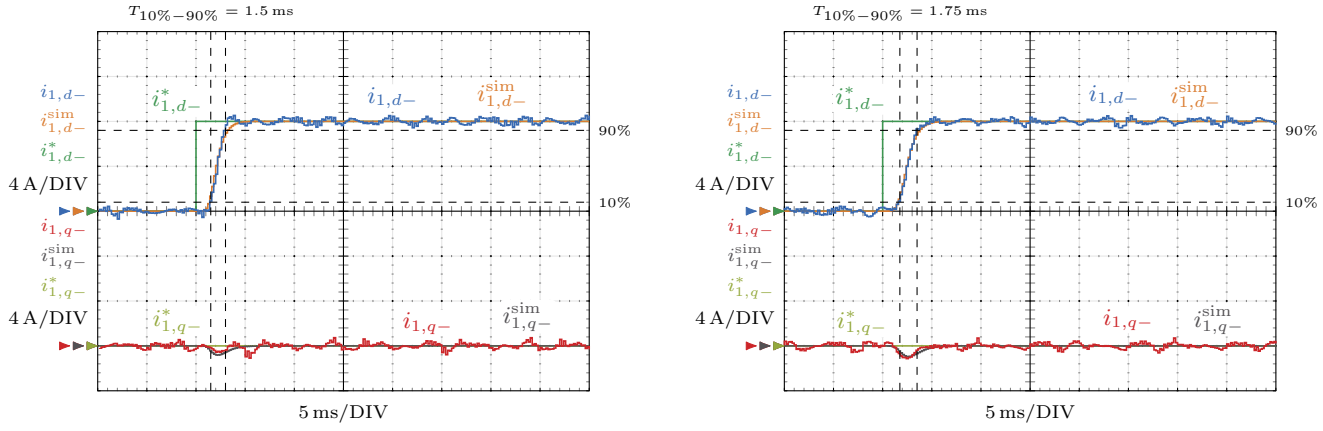

(a) (b)

Fig. 12. Experimental and simulation waveforms ($i_{1,dq}$ and $i^{\text{sim}}_{1,dq}$, respectively) for a reference step $i^{*}_{1,q-}$ in the negative synchronous frame dq− rotating at the fundamental grid frequency ω_g. (a) LCL filter I (b) LCL filter II.

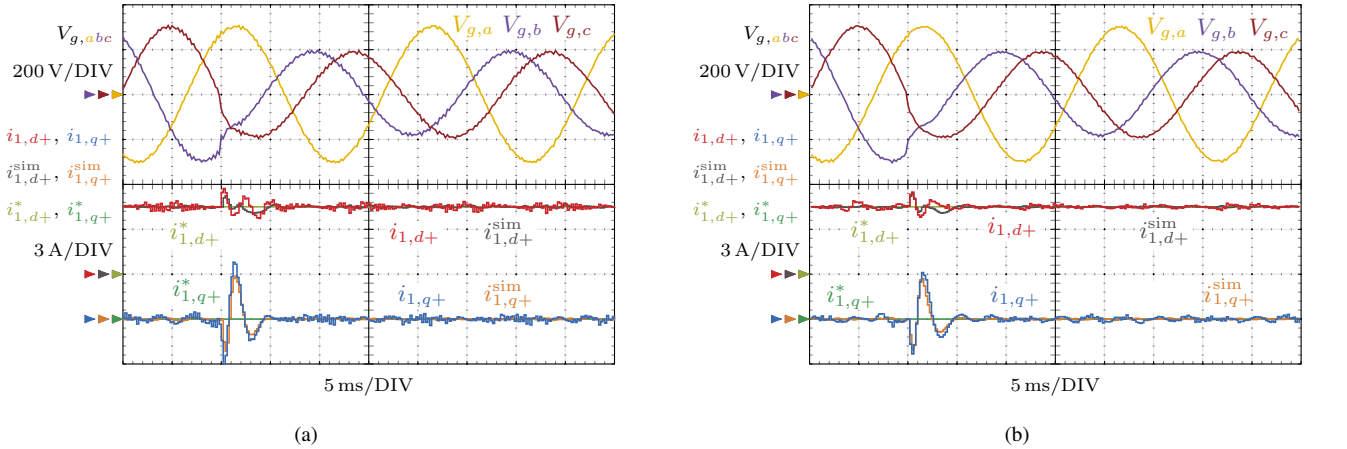

(a) (b)

Fig. 13. Experimental and simulation waveforms ($i_{1,dq}$ and $i^{\text{sim}}_{1,dq}$, respectively) for a 40%-depth type-C sag in $V_{g,abc}$ while keeping the reference $i^{*}_{1,dq}$ constant. (a) LCL filter I. (b) LCL filter II.

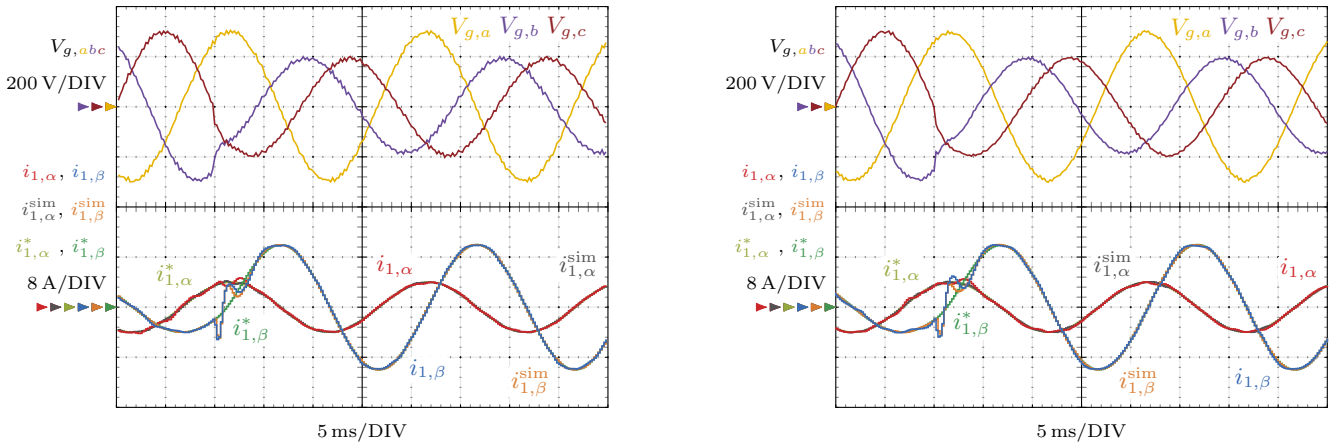

Fig. 14. Experimental and simulation waveforms ($i_{1,\alpha\beta}$ and $i^{\text{sim}}_{1,\alpha\beta}$, respectively) for a 40%-depth type-C sag in $V_{g,abc}$. The reference step i^{*}_{1} is calculated according to the so-called positive-negative-sequence compensation strategy [31]. (a) LCL filter I. (b) LCL filter II.

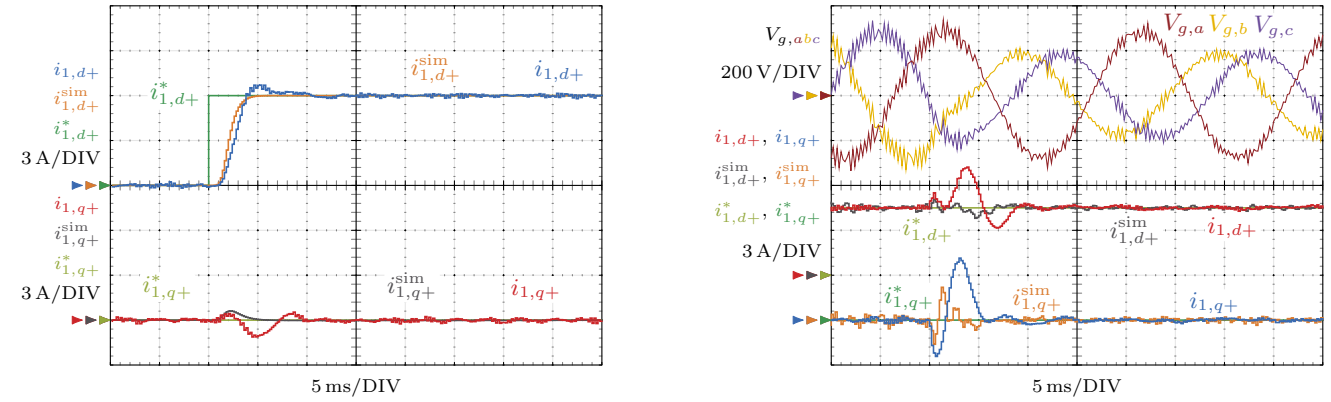

Fig. 15. Experimental, simulation, and reference waveforms ($i_{1,dq}$, $i^{\text{sim}}_{1,dq}$, and $i^{*}_{1,q+}$, respectively) in the positive synchronous frame dq+ when the converter is connected to a weak grid and the LCL filter I is installed. (a) A reference step. (b) A 40%-depth type-C voltage sag in $V_{g,abc}$.

to within 2% makes it possible to evaluate the time required by the current controller to recover from a sag disturbance. A value of settling time $t_{\text{st}} = 4\,\text{ms}$ is obtained, which is slightly greater (but still short) than the $t_{\text{st}} = 4/(2\pi f_{\text{dom}})$ of a first-order system; this is due to the effect of the extra non-dominant closed-loop poles. The next test (Fig. 14) evaluates the reference-tracking capability under the same sag. A reference step i^{*}_{1} is generated according to the positive-negative-sequence compensation strategy [31]. Since the currents now have a positive and a negative sequence, they are shown in stationary frame. A fast and well damped response is also obtained when both effects are combined.

In the previous tests, it can be seen that the transient-response parameters (rise time, overshoot, and settling time) are determined by the selected dominant natural frequency f_{dom}, defined during the design process. They do not depend on the LCL filter resonant frequency. The oscilloscope captures obtained with filter I ($f_{\text{res}} < f_{\text{s}}/6$), shown in Figs. 11(a)–14(a) display similar transient characteristics to those made with filter II ($f_{\text{res}} > f_{\text{s}}/6$), shown in Figs. 11(b)–14(b).

Finally, an experimental test was carried out to assess the robustness of the controller when connected to a weak grid. The weak grid has an impedance of value $Z_g = 0.15 + j0.10\,\text{p.u.}$, which is one of the values analyzed in Section IV, cf. Fig. 9(e). The test is composed of two parts. In Fig. 15(a), a reference step is commanded to test the reference-tracking response and, in Fig. 15(a), the disturbance rejection is tested under the same voltage sag as in Fig. 13. The responses are not significantly modified compared to Figs. 11 and 13. In conclusion, the stability of the system is preserved even with substantial deviations in the plant parameters. This behavior is in accordance with the theoretical analysis presented in Section IV.

VI. Conclusion

This paper has presented an enhanced current RC for grid-tied converters with LCL filter. The developed method is based on direct discrete-time pole placement from the classical

control theory, involving two extra filters. It provides a simple design process of the controller for a wide range of LCL filter values and it ensures stable operation without additional damping methods. The available bandwidth is examined in order to define the frequency of the dominant pole in the system. As a result, a fast reference-tracking capability with negligible overshoot and low controller effort are attained in combination with a fast disturbance rejection. The sensitivity to variations in the grid inductance is low due to the proposed pole-placement strategy.

The proposed controller also has the well-known characteristics of the conventional RCs, e.g., zero steady-state error at both fundamental sequences, and a simple implementation with a low computational load compared to state-space controllers from modern control theory.

The design was validated with both simulations and experiments.

Appendix A
Pole-Placement Equations to Locate the Poles at the Desired Locations From Table I

The augmented plant model (i.e., including the RC) in (6) has order six and a relative degree of four:

$$G_3(z) = \frac{B(z)}{A(z)} \tag{19}$$

where

$$\begin{aligned} A(z) &= a_6 z^6 + a_5 z^5 + a_4 z^4 + a_3 z^3 + a_2 z^2 + a_1 z + 0 \\ B(z) &= b_2 z^2 + b_1 z + b_0. \end{aligned} \tag{20}$$

The $C(z)$ controller transfer function is

$$C(z) = \frac{M(z)}{N(z)}. \tag{21}$$

This controller permits to obtain the ten coefficients of the desired system characteristic polynomial A_{cl} according to the closed-loop pole locations defined in Section III:

$$\begin{aligned} A_{cl} &= A(z)N(z) + B(z)M(z) \\ &= d_9 z^9 + d_8 z^8 + d_7 z^7 + d_6 z^6 + d_5 z^5 \\ &\quad + d_4 z^4 + d_3 z^3 + d_2 z^2 + d_1 z + d_0 \end{aligned} \tag{22}$$

where the roots of the characteristic polynomial are the desired closed-loop poles of the system from Table I:

$$A_{cl} = (z - p_1^{cl})(z - p_2^{cl}) \cdots (z - p_9^{cl}).$$

To reduce the order of the complete system, the controller $C(z)$ is designed to have the lowest order possible. $C(z)$ can have a negative relative degree of two (which gives the minimum order achievable for the system) because the complete controller $C(z)C_{\mathrm{RC}}(z)$ is still proper.

Hence, since the controller $C(z)$ has ten parameters and a negative relative degree of two, the following two polynomials [which give a third-order transfer function for $C(z)$] are obtained:

$$\begin{aligned} M(z) &= m_5 z^5 + m_4 z^4 + m_3 z^3 + m_2 z^2 + m_1 z + m_0 \\ N(z) &= n_3 z^3 + n_2 z^2 + n_1 z + n_0. \end{aligned} \tag{23}$$

The polynomial Diophantine equation in (22) can be expressed in matrix notation as

$$Sc = d \tag{24}$$

where

$$S = \begin{bmatrix} a_6 & 0 & 0 & 0 & 0 & 0 & 0 & 0 & 0 & 0 \\ a_5 & a_6 & 0 & 0 & 0 & 0 & 0 & 0 & 0 & 0 \\ a_4 & a_5 & a_6 & 0 & b_2 & 0 & 0 & 0 & 0 & 0 \\ a_3 & a_4 & a_5 & a_6 & b_1 & b_2 & 0 & 0 & 0 & 0 \\ a_2 & a_3 & a_4 & a_5 & b_0 & b_1 & b_2 & 0 & 0 & 0 \\ a_1 & a_2 & a_3 & a_4 & 0 & b_0 & b_1 & b_2 & 0 & 0 \\ 0 & a_1 & a_2 & a_3 & 0 & 0 & b_0 & b_1 & b_2 & 0 \\ 0 & 0 & a_1 & a_2 & 0 & 0 & 0 & b_0 & b_1 & b_2 \\ 0 & 0 & 0 & a_1 & 0 & 0 & 0 & 0 & b_0 & b_1 \\ 0 & 0 & 0 & 0 & 0 & 0 & 0 & 0 & 0 & b_0 \end{bmatrix}$$

$$\begin{aligned} c &= \begin{bmatrix} n_3 & n_2 & n_1 & n_0 & m_5 & m_4 & m_3 & m_2 & m_1 & m_0 \end{bmatrix}^{\mathrm{T}} \\ d &= \begin{bmatrix} d_9 & d_8 & d_7 & d_6 & d_5 & d_4 & d_3 & d_2 & d_1 & d_0 \end{bmatrix}^{\mathrm{T}}. \end{aligned} \tag{25}$$

Therefore, the coefficients of the controller $C(z)$ that place the closed-loop poles at the desired locations are obtained by solving this system of linear equations:

$$c = S^{-1} d. \tag{26}$$

Appendix B
Computational Load

The computational load of the proposed transfer function controller is analyzed in number of operations and compared with an equivalent state-space controller. This is commonly regarded as valid for assessing the computational burden without further experimental verification [32].

The proposed controller implements two transfer functions, which are the prefilter and the loop filter. The prefilter (12) is a second-order transfer function with a relative degree of one (the difference between the number of poles and the number of zeros). The loop filter is the product of $C_{\mathrm{RC}}(z)$ [cf. (5)] times $C(z)$ [cf. (21) and (23)]. This yields a strictly-proper (the same number of poles and zeros) fifth-order transfer function. The computational load required by a discrete transfer function is proportional to the number of coefficients. Each coefficient requires a multiplication of a complex variable by a real coefficient and a complex addition to be performed. At most, the number of coefficients in a transfer function is equal to the number of poles and zeros plus two. A multiplication requires two floating-point operations (flops) and a complex addition is performed in two flops. Therefore, this controller has a constant complexity of 34 flops. The total number of flops per second that the proposed current controller executes is $34 f_{\mathrm{s}}$. In the presented implementation ($f_{\mathrm{s}} = 5$ kHz), a figure of 170 kilo-flops per second is obtained.

A proper transfer function is that in which the degree of the numerator does not exceed the degree of the denominator [26]. This ensures that the system is causal and can be implemented in a real control device.

Sylvester's theorem [27] ensures that S is invertible.

On the other hand, the state space controller in [24] requires the implementation of an observer and a control law. The observer equation is

$$\begin{aligned}\hat{\mathbf{x}}_\mathbf{b}(k) = &\underbrace{(\mathbf{F_{bb}} - \mathbf{K_o F_{ab}})}_{5\times5}\underbrace{\hat{\mathbf{x}}_\mathbf{b}(k-1)}_{5\times1} \\ &+ \underbrace{\mathbf{K_o}}_{5\times1}\underbrace{i_1(k)}_{1\times1} + \underbrace{(\mathbf{F_{ba}} - \mathbf{K_o}F_{aa})}_{5\times1}\underbrace{i_1(k-1)}_{1\times1} \\ &+ \underbrace{(\mathbf{G_b} - \mathbf{K_o}G_a)}_{5\times1}\underbrace{u(k-1)}_{1\times1}. \end{aligned} \quad (27)$$

The control law equation is

$$u(k) = \underbrace{K_f}_{1\times1}\underbrace{i_1^*}_{1\times1} - \underbrace{\begin{bmatrix}\mathbf{K_c} & 1 & 0\end{bmatrix}}_{1\times6}\underbrace{\begin{bmatrix} i_1 \\ \hat{\mathbf{x}}_\mathbf{b}\end{bmatrix}}_{6\times1}. \quad (28)$$

Therefore, the number of operations that this controller requires is 47 multiplications of complex variables by real coefficients and 47 complex additions. This results in a constant complexity of 188 flops ($188 f_s$-flops per second).

As a consequence, the computational load of the proposed controller is less than five times that of [24], which makes the former particularly suited for an implementation in a embedded controller when a high switching frequency is required.

REFERENCES

[1] B. K. Bose, "Global energy scenario and impact of power electronics in 21st century," *IEEE Trans. Ind. Electron.*, vol. 60, no. 7, pp. 2638–2651, Jul. 2013.

[2] R. Grünbaum, "Voltage and power quality control in wind power," in *Proc. Powergen Europe, Brussels*, 2001.

[3] A. Vidal, F. D. Freijedo, A. G. Yepes, J. Malvar, O. López, and J. Doval-Gandoy, "Transient response evaluation of stationary-frame resonant current controllers for grid-connected applications," *IET Power Electron.*, vol. 7, no. 7, pp. 1714–1724, Jul. 2014.

[4] M. P. Bahrman, J. G. Johansson, and B. A. Nilsson, "Voltage source converter transmission technologies: the right fit for the application," in *Proc. IEEE Power Eng. Soc. Gen. Meeting*, vol. 3, Jul. 2003, p. 1847 Vol. 3.

[5] P. Channegowda and V. John, "Filter optimization for grid interactive voltage source inverters," *IEEE Trans. Ind. Electron.*, vol. 57, no. 12, pp. 4106–4114, Dec. 2010.

[6] G. Shen, X. Zhu, J. Zhang, and D. Xu, "A new feedback method for PR current control of LCL-filter-based grid-connected inverter," *IEEE Trans. Ind. Electron.*, vol. 57, no. 6, pp. 2033–2041, Jun. 2010.

[7] A. G. Yepes, F. D. Freijedo, O. López, and J. Doval-Gandoy, "Analysis and design of resonant current controllers for voltage-source converters by means of Nyquist diagrams and sensitivity function," *IEEE Trans. Ind. Electron.*, vol. 58, no. 11, pp. 5231–5250, Nov. 2011.

[8] C. Citro, P. Siano, and C. Cecati, "Designing inverters' current controllers with resonance frequencies cancellation," *IEEE Trans. Ind. Electron.*, vol. 63, no. 5, pp. 3072–3080, May 2016.

[9] L. Harnefors, A. G. Yepes, A. Vidal, and J. Doval-Gandoy, "Passivity-based controller design of grid-connected VSCs for prevention of electrical resonance instability," *IEEE Trans. Ind. Electron.*, vol. 62, no. 2, pp. 702–710, Feb. 2015.

[10] S. G. Parker, B. P. McGrath, and D. G. Holmes, "Regions of active damping control for LCL filters," *IEEE Trans. Ind. Appl.*, vol. 50, no. 1, pp. 424–432, Jan./Feb. 2014.

[11] L. Huang, B. Li, Z. Lu, L. Hang, and L. Tolbert, "PR controller for grid-connected inverter control using direct pole placement strategy," in *Proc. IEEE ISIE*, May 2012, pp. 469–474.

[12] Y. Jia, J. Zhao, and X. Fu, "Direct grid current control of LCL-filtered grid-connected inverter mitigating grid voltage disturbance," *IEEE Trans. Power Electron.*, vol. 29, no. 3, pp. 1532–1541, Mar. 2014.

[13] H. Komurcugil, N. Altin, S. Ozdemir, and I. Sefa, "Lyapunov-function and proportional-resonant-based control strategy for single-phase grid-connected VSI with LCL filter," *IEEE Trans. Ind. Electron.*, vol. 63, no. 5, pp. 2838–2849, May 2016.

[14] B. Li, W. Yao, L. Hang, and L. M. Tolbert, "Robust proportional resonant regulator for grid-connected voltage source inverter (VSI) using direct pole placement design method," *IET Power Electron.*, vol. 5, no. 8, pp. 1367–1373, Sep. 2012.

[15] D. Pan, X. Ruan, C. Bao, W. Li, and X. Wang, "Optimized controller design for LCL-type grid-connected inverter to achieve high robustness against grid-impedance variation," *IEEE Trans. Ind. Electron.*, vol. 62, no. 3, pp. 1537–1547, Mar. 2015.

[16] X. Wang, F. Blaabjerg, and P. C. Loh, "Grid-current-feedback active damping for LCL resonance in grid-connected voltage-source converters," *IEEE Trans. Power Electron.*, vol. 31, no. 1, pp. 213–223, Jan. 2016.

[17] J. Xu, S. Xie, and T. Tang, "Active damping-based control for grid-connected LCL-filtered inverter with injected grid current feedback only," *IEEE Trans. Ind. Electron.*, vol. 61, no. 9, pp. 4746–4758, Sep. 2014.

[18] L. Harnefors, A. G. Yepes, A. Vidal, and J. Doval-Gandoy, "Passivity-based stabilization of resonant current controllers with consideration of time delay," *IEEE Trans. Power Electron.*, vol. 29, no. 12, pp. 6260–6263, Dec. 2014.

[19] A. Vidal, A. G. Yepes, F. D. Freijedo, J. Malvar, O. López, and J. Doval-Gandoy, "A technique to estimate the equivalent loss resistance of grid-tied converters for current control analysis and design," *IEEE Trans. Power Electron.*, vol. 30, no. 3, pp. 1747–1761, Mar. 2015.

[20] C. A. Busada, S. G. Jorge, and J. A. Solsona, "Resonant current controller with enhanced transient response for grid-tied inverters," *IEEE Trans. Ind. Electron.*, accepted for publication.

[21] R. Peña-Alzola, M. Liserre, F. Blaabjerg, R. Sebastián, J. Dannehl, and F. W. Fuchs, "Analysis of the passive damping losses in LCL-filter-based grid converters," *IEEE Trans. Power Electron.*, vol. 28, no. 6, pp. 2642–2646, Jun. 2013.

[22] Y. Tang, P. C. Loh, P. Wang, F. H. Choo, F. Gao, and F. Blaabjerg, "Generalized design of high performance shunt active power filter with output LCL filter," *IEEE Trans. Ind. Electron.*, vol. 59, no. 3, pp. 1443–1452, Mar. 2012.

[23] M. Hanif, V. Khadkikar, W. Xiao, and J. L. Kirtley, "Two degrees of freedom active damping technique for LCL filter-based grid connected PV systems," *IEEE Trans. Ind. Electron.*, vol. 61, no. 6, pp. 2795–2803, Jun. 2014.

[24] D. Pérez-Estévez, J. Doval-Gandoy, A. G. Yepes, and O. López, "Positive- and negative-sequence current controller with direct discrete-time pole placement for grid-tied converters with LCL Filter," *IEEE Trans. Power Electron.*, vol. 32, no. 9, pp. 7207–7221, Sep. 2017.

[25] C. A. Busada, S. Gomez Jorge, and J. A. Solsona, "Full-state feedback equivalent controller for active damping in LCL-filtered grid-connected inverters using a reduced number of sensors," *IEEE Trans. Ind. Electron.*, vol. 62, no. 10, pp. 5993–6002, Oct. 2015.

[26] G. F. Franklin, J. D. Powell, and M. L. Workman, *Digital Control of Dynamic Systems*, 3rd ed. Addison Wesley Longman, Inc, 1998, pp. 202–203, 110, 322–336, 308–309, 400–403, 289–301, 286.

[27] G. C. Goodwin, S. F. Graebe, and M. E. Salgado, *Control System Design*, 1st ed. Prentice Hall, 2001.

[28] K. J. Astrom, P. Hagander, and J. Sternby, "Zeros of sampled systems," *Automatica*, vol. 20, no. 1, pp. 31 – 38, 1984.

[29] M. Liserre, F. Blaabjerg, and S. Hansen, "Design and control of an LCL-filter-based three-phase active rectifier," *IEEE Trans. Ind. Appl.*, vol. 41, no. 5, pp. 1281–1291, Sep./Oct. 2005.

[30] M. H. Bollen, *Understanding Power Quality Problems: Voltage Sags and Interruptions*, 1st ed. Wiley, 1999, p. 194.

[31] P. Rodriguez, A. V. Timbus, R. Teodorescu, M. Liserre, and F. Blaabjerg, "Flexible active power control of distributed power generation systems during grid faults," *IEEE Trans. Ind. Electron.*, vol. 54, no. 5, pp. 2583–2592, Oct. 2007.

[32] I. Etxeberria-Otadui, A. L. D. Heredia, H. Gaztanaga, S. Bacha, and M. R. Reyero, "A single synchronous frame hybrid (SSFH) multifrequency controller for power active filters," *IEEE Trans. Ind. Electron.*, vol. 53, no. 5, pp. 1640–1648, Oct. 2006.

Diego Pérez-Estévez (S'15) received the M.Sc. degree in telecommunications engineering, in 2014, from the University of Vigo, Vigo, Spain, where he is currently working toward the Ph.D. degree in the Applied Power Electronics Technology Research Group.

Since 2014, he has been with the Applied Power Electronics Technology Research Group. His research interests include control of grid-connected converters and distributed power generation systems.

Jesús Doval-Gandoy (M'99) received the M.Sc. degree from the Polytechnic University of Madrid, Madrid, Spain, in 1991 and the Ph.D. degree in electrical engineering from the University of Vigo, Vigo, Spain in 1999.

From 1991 till 1994 he worked at industry. He is currently the head of the Applied Power Electronics Technology Research Group, University of Vigo. His research interests are in the areas of ac power conversion.

Alejandro G. Yepes (S'10-M'12) received the M.Sc. and Ph.D. degrees in electrical engineering from the University of Vigo, Vigo, Spain in 2009 and 2011, respectively.

Since 2008, he has been with the Applied Power Electronics Technology Research Group, University of Vigo. His research interests are in the areas of ac power conversion, with special focus, currently, on multiphase drives and digital control of power electronics converters.

Oscar López (M'05-SM'16) received the M.Sc. and Ph.D. degrees in electrical engineering from the University of Vigo, Vigo, Spain, in 2001 and 2009, respectively.

Since 2004, he has been an Assistant Professor at the University of Vigo. He is a member of the Applied Power Electronics Technology Research Group, University of Vigo. His research interests include the areas of ac power switching converters technology.

Fernando Baneira (S'15) received the M.Sc. degree in electrical engineering from the University of Vigo, Vigo, Spain, in 2013, where he has been working toward the Ph.D. degree in the Applied Power Electronics Technology Research Group since 2014.

His research interests include power electronics, multiphase systems, and ac drives.